PAPER

Directional effect on the fusion of ellipsoidal morphologies into nanorods and nanotubes†

Yahui Li,[a] Qunzan Lu,[b] Qiumeng Chen,[a] Xuan Wu,[b] Jianliang Shen [ID] *[ab] and Liangliang Shen [ID] *[a]

Particle fusion is well-recognized as an important spontaneous process to produce higher-order nanostructures during morphology transition in polymerization-induced self-assembly (PISA). However, to our knowledge, the directional contact, adhesion, and fusion of adjacent nanoparticles have been rarely elucidated in PISA. Herein, a directional fusion of ellipsoidal morphologies was demonstrated during PISA of semi-fluorinated liquid-crystalline (SFLC) block copolymers. The ellipsoidal nanostructures, including micelles and vesicles, preferred to undergo a directional fusion in a head-to-head model, leading to the formation of nanorods and nanotubes, respectively. We believe the directional fusion will offer insightful guidance in PISA to the preparation of complicated functional nanostructures.

Introduction

Over the past few decades, the solution self-assembly of block copolymers (BCPs) as a versatile approach to constructing nanostructures has been greatly developed.[1–9] However, traditional self-assembly of BCPs suffers from recognized limitations, such as a low concentration (below 1 wt% solids) and multiple-step process,[1,10] which severely impede the scalable production of BCP nanomaterials. In contrast, polymerization-induced self-assembly (PISA) *via* reversible addition–fragmentation chain transfer (RAFT)-mediated dispersion polymerization has been well-established as a reliable strategy for efficient production of BCP nanoparticles with tailorable properties.[11–17] During a typical dispersion polymerization, a stabilizer homopolymer is chain-extended by polymerizing a soluble monomer to produce amphiphilic BCPs, which *in situ* self-assemble to form nanoparticles with diverse morphologies. The morphology evolution during PISA has been systematically investigated, providing guiding principles for predicting BCP morphologies. Generally, in a typical PISA process, the spheres fused into worms, lamellas, and all the way to high-order vesicles with the growth of core-forming blocks.[18] As a consequence, the formation of nanorods and nanotubes is highly sensitive to synthetic conditions such as solids contents, polymerization solvents,

and block compositions.[19] Although a few researchers have developed novel PISA strategies for polymeric worms, nanowires, and nanotubes,[20–26] it is still challenging to produce nanorods and nanotubes through the self-assembly of amorphous coil–coil BCPs.

Recently, liquid-crystalline (LC) block copolymers have been broadly employed to mediate the self-assembly behaviors of BCPs. In particular, it was well-demonstrated that self-assembly of LC block copolymers facilitated the formation of cylindrical nanostructures.[27,28] For example, Li and co-workers found that BCPs comprising a cholesteryl LC core-forming block preferred to form cylindrical micelles.[29] Winnik *et al.* described that the self-assembly of BCPs comprising a polyferrocenylsilane block can readily produce rod-like micelles within a broad range of BCP composition window.[30] Among various liquid-crystalline polymers, fluorinated polymers are remarkable materials because of their unique properties and wide applications in several areas.[29–33] Particularly, semi-fluorinated poly(meth)acrylates bearing side groups with high numbers of fluorocarbons (≥7) exhibit excellent LC nature because F-alkyl chains are much bulkier and more rigid than alkyl chains.[34,35] In recent years, the self-assembly of semi-fluorinated liquid-crystalline (SLFC) BCPs for constructing cylindrical nanostructures has been systematically developed. For example, Liu and co-workers demonstrated that triblock terpolymers bearing a fluorinated block can readily self-assemble into cylindrical micelles.[36] Manners *et al.* reported that the self-assembly of a SLFC BCP afforded monodisperse cylindrical micelles through a fragmentation-thermal annealing process.[37] Yuan and co-workers found that cylindrical micelles could be readily prepared by PISA of semi-fluorinated-containing monomer in a wide range of lengths of core-forming block.[38] However, the dynamic process

[a] State Key Laboratory of Ophthalmology, Optometry and Vision Science, School of Ophthalmology and Optometry, School of Biomedical Engineering, Wenzhou Medical University, Wenzhou 325027, PR China. E-mail: shenjl@wiucas.ac.cn

[b] Engineering Research Center of Clinical Functional Materials and Diagnosis & Treatment Devices of Zhejiang Province, Wenzhou Institute, University of Chinese Academy of Sciences, Xinsan Road, Longwan District, Wenzhou 325001, PR China

of morphology evolution for the formation of cylindrical micelles was not discussed. Despite significant progress, the unique advantage of BCPs with a LC block in forming cylindrical nanostructures compared with coil–coil BCPs need further elucidation.

Recently, a few researchers have reported that ellipsoidal morphologies can be readily obtained through PISA of rigid rod-coil BCPs with a LC block.[39] For instance, Chen and co-workers presented an efficient approach to forming a series of anisotropic morphologies, including ellipsoidal vesicles *via* polymerization-induced hierarchical self-assembly of azobenzene-containing BCPs.[40] Shen and co-workers reported that facile preparation of ellipsoidal micelles can be achieved in the dispersion polymerization of heptadecafluorodecyl methacrylate (HDFDMA) employing several macromolecular chain transfer agents (macro-CTAs) in a wide selection of solvents.[41] In contrast, the PISA of amorphous coil–coil BCPs usually results in isotropic spheres.

Fusion is an important spontaneous process to generate higher-order structures during morphology evolution in PISA.[42] For instance, spheres fuse to worms[18] and vesicles fuse to form tubes, compound vesicles,[43] and tetrapod polymersomes.[44] Cai and co-workers have well-demonstrated that one-dimensional nanowires readily formed *via* the fusion of spindle-like micelles along the long axis of the micelles.[45,46] We envision that it might also undergo a directional fusion of ellipsoidal morphologies during the formation of cylindrical nanostructures *via* PISA of BCPs containing a LC block. However, to the best of our knowledge, the directional fusion effect on the formation of cylindrical nanostructures has been rarely discussed in PISA. Although Lv *et al.* reported that the fusion of vesicles in one dimension can occur to form nanotubes in their PISA protocol,[43] the directional contact, adhesion, and fusion of adjacent nanoparticles was not elucidated. Herein, we aim to verify the directional effect on the fusion of ellipsoidal morphologies during dispersion polymerization of HDFDMA using poly(2-(dimethylamino)ethyl methacrylate) (PDMAEMA$_{30}$) as the macro-CTA.

Results and discussion

As demonstrated in Scheme 1A, a PDMAEMA$_{30}$ macro-CTA was employed to mediate the reversible addition–fragmentation chain transfer (RAFT) dispersion polymerization of HDFDMA. The PDMAEMA$_{30}$-CTA was first synthesized *via* RAFT homogeneous polymerization of DMAEMA in *N,N*-dimethylformamide (DMF) at 70 °C. After dialysis against ethanol for two days, the degree of the polymerization (DP) of DMAEMA was calculated to be 30 by comparing the integral ratio of signal *h* (δ = 4.09 ppm) and *b* (δ = 3.27 ppm) (Fig. 1A). GPC analysis in Fig. 1B shows a narrow molecular weight distribution (M_w/M_n = 1.12) and good agreement between theoretical and experimental molecular weights ($M_{n,NMR}$ = 4973 g mol^{-1}, $M_{n,GPC}$ = 5077 g mol^{-1}), indicating good control of molecular weight distributions.

Then, the PDMAEMA$_{30}$ macro-CTA was chain-extended through RAFT dispersion polymerization of HDFDMA in ethanol at 70 °C at 20% w/v solids content. The polymerization
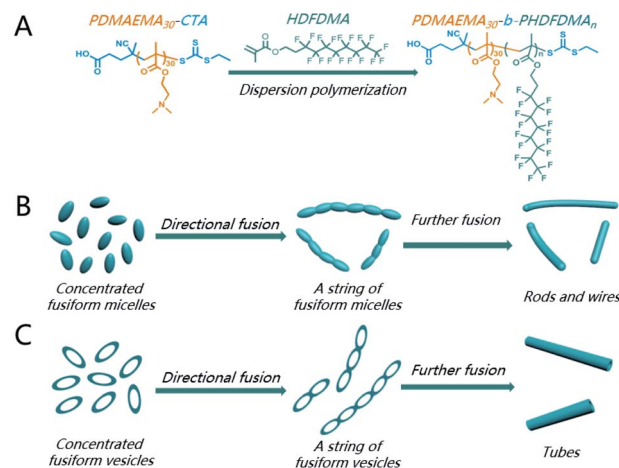
Scheme 1 (A) RAFT PISA process for BCPs nano-objects containing a SFLC block *via* chain-extension of PDMAEMA$_{30}$ macro-CTA; (B) formation of nanorods through the directional fusion of ellipsoidal micelles and (C) formation of nanotubes through the directional fusion of ellipsoidal vesicles.
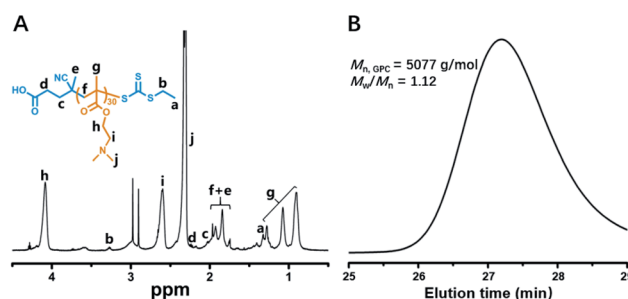

Fig. 1 ^{1}H NMR spectrum (A) and GPC trace (B) of PDMAEMA$_{30}$ macro-CTA.

condition and results were summarized in Table 1. ^{1}H NMR spectra confirmed that near quantitative HDFDMA conversions were accomplished within 11–23 h. The BCPs compositions can

Table 1 Summary of the dispersion polymerization of HDFDMA in ethanol mediated by PDMAEMA$_{30}$-CTA at 70 °C

Feed ratio[a]	Solids%	Conv.[b]%	$D_{h,app}$[c]	PDI[c]
1/50/0.3	20	99	126	0.18
1/60/0.3	20	99	140	0.11
1/70/0.3	20	99	164	0.08
1/80/0.3	20	99	191	0.08
1/90/0.5	20	99	200	0.15
1/100/0.5	20	99	280	0.43
1/100/0.5	15	99	230	0.34
1/100/0.5	30	99	350	0.49
1/105/0.5	30	99	618	0.35

[a] Molar ratio (PDMAEMA$_{30}$-CTA/HDFDMA/AIBN). [b] Monomer conversions determined by ^{1}H NMR spectroscopy in CDCl$_3$. [c] The average value of apparent hydrodynamic diameter ($D_{h,app}$) and the polydispersity index (PDI) of particle size confirmed by DLS characterizations with the block copolymer concentration of 0.1% (1 mg mL^{-1}).
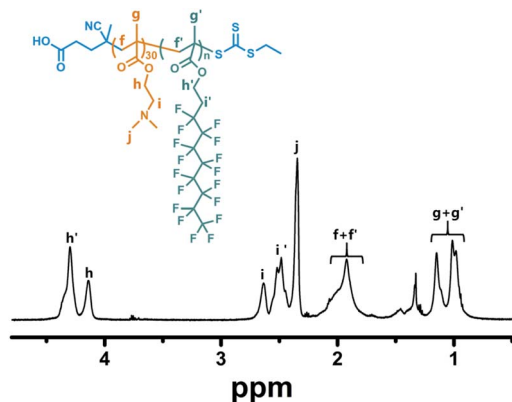
Fig. 2 ^{1}H NMR spectrum of PDMAEMA$_{30}$–PHDFDMA$_{62}$ block copolymer in CDCl$_3$/CF$_2$ClCFCl$_2$ mixed solvent (3 : 2, v/v). The targeting DP of HDFDMA was 60.

Fig. 4 DLS results of PDMAEMA$_{30}$–PHDFDMA$_n$ BCP nano-objects synthesized *via* PISA in ethanol at varied solids content.

be confirmed by ^{1}H NMR using a mixed solution CDCl$_3$/CF$_2$-ClCFCl$_2$ (3 : 2, v/v), which allowed efficient dissociation of SFLC block aggregation and ordering. Fig. 2 demonstrated the ^{1}H NMR spectrum of PDMAEMA$_{30}$–PHDFDMA$_{62}$ as a representative example. Although the targeting DP of HDFDMA was 60, the actual repeat units of HDFDMA was determined to be 62 by comparing the integral ratio of signal h' (δ = 4.30 ppm) and h (δ = 4.14 ppm).

The morphologies of BCP nanostructures were analysed by transmission electron microscopy (TEM). The corresponding size distributions of the PDMAEMA$_{30}$–PHDFDMA$_n$ nano-objects were characterized by dynamic light scattering (DLS). As shown in Fig. 3A, the dispersion polymerization targeting a DP of 50 resulted in a mixture of anisotropic ellipsoidal micelles with different sizes. The DLS results in Fig. 4 (the black line) indicated an average value of the apparent hydrodynamic diameter
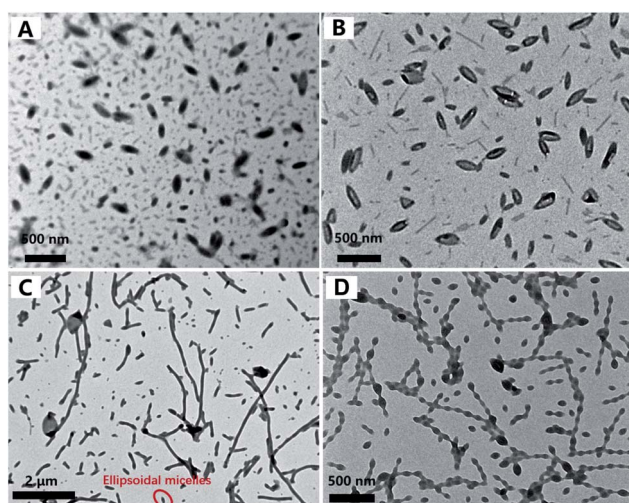
($D_{\text{h,app}}$) at 126 nm with PDI = 0.18. The statistical analysis in Fig. S1† indicated that the average length of short and long axis for big ellipsoidal micelles is 91 and 212 nm, respectively. As for small ellipsoidal micelles, the average length of the short and long axis was determined to be 40 and 96 nm, respectively. As the targeting DP increased to 60, the average $D_{\text{h,app}}$ of the nanoobjects slightly increased to be 140 nm with PDI of 0.11 (the red line in Fig. 4). The TEM image in Fig. 3B indicated that ellipsoidal vesicles in coexistence with short rods generated. The statistical analysis in Fig. S2A and B† indicated that the average length of the short and long axis of the ellipsoidal vesicles is about 225 nm and 95 nm, respectively. The average thickness of the vesicular wall is calculated to be 36 nm (Fig. S2C†). The average width of short rods (30 nm, Fig. S2E†) is slightly lower than the short axis of small ellipsoidal micelles (40 nm on average, Fig. S1D†), indicating that short rods were generated from the fusion of small ellipsoidal micelles. As shown in Fig. S3,† the near-ellipsoidal vesicles with varied size formed when the DP of HDFDMA was targeted as 70, 80, and 90, respectively. Besides the near-ellipsoidal vesicles, ellipsoidal micelles with small size can also be observed. Their corresponding DLS results were exhibited in Fig. S4.†

Interestingly, with a further increase of DP of HDFDMA to 100, nanorods with varied length formed (Fig. 3C). Besides nanorods, ellipsoidal micelles can also be clearly observed. DLS results in Fig. 4 (the blue line) also demonstrated a wide distribution of size (PDI = 0.43). The peak at 1189 nm corresponded to long rods while the peak at 177 nm corresponded to the mixture of short rods and ellipsoidal micelles. The statistical analysis in Fig. S5† demonstrated that the average width of nanorods (108 nm) is basically consistent with the short axis of the ellipsoidal micelles, suggesting that nanorods were resulted from the directional fusion of the ellipsoidal micelles along the long axis. As is well-recognized, the solids content is one of the critical factors influencing the morphology evolution process in PISA. In principle, low solid contents will retard the morphology evolution by decreasing the probability of collision and fusion of nanoparticles.[47–49] To acquire more convincing evidence for a directional fusion of ellipsoidal micelles, the PISA of

Fig. 3 TEM micrographs of PDMAEMA$_{30}$–PHDFDMA$_n$ nano-objects synthesized *via* PISA: (A) ellipsoidal micelles, n = 50, 20% solids content; (B) ellipsoidal vesicles, n = 60, 20% solids content; (C) nanorods, n = 100, 20% solids content and (D) a string of ellipsoidal micelles, n = 100, 15% solids content.
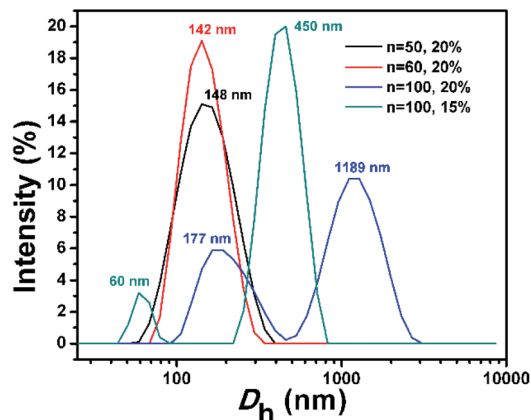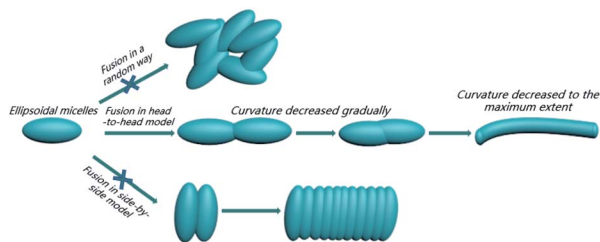
PDMAEMA$_{30}$–PHDFDMA$_{100}$ at 15% solids content was subsequently performed. As shown in Fig. 3D, a string of ellipsoidal micelles as an intermediate state into long rods is successfully captured. DLS result in Fig. 4 (the green line) exhibited two main peaks at 60 and 450 nm, respectively, which is in good agreement with the corresponding TEM image in Fig. 3D. Moreover, the adjacent ellipsoidal micelles are linked together along the long axis. This result confirms our hypothesis that the directional fusion of ellipsoidal micelles along their long axis can lead to the formation of nanorods, which is schematically illustrated in Scheme 1B. Similarly, Cai *et al.* elucidated that partial open ends exist in the ellipsoidal-like particles due to the uneven coverage of the particle core by the stabilizer chains, leading to particle fusion in a head-to-head model.[45]

As well-elucidated, the membrane curvature serves as a critical factor in dictating the morphology transition of BCPs nanoparticles.[18,50] Particle fusion during PISA is mainly driven by membrane tension.[42] Therefore, one of the motivations for the morphology transition is to reduce the membrane curvature and tension to the maximum extent. The fusion of the spherical micelles into worm-like micelles is isotropic since the molecular curvature for spherical micelles is isotropic. In contrast, the membrane curvature of the ellipsoidal micelles is anisotropic: the membrane curvature of the two poles is much higher than other locations. Theoretically, three kinds of fusion models of ellipsoidal nanoparticles can be presented, which can be denoted as a head-to-head model, a side-by-side model, and a random model, respectively (Scheme 2). As revealed by TEM analysis in Fig. 3D, the ellipsoidal micelles preferred to fuse in a head-to-head model, affording the lowest membrane curvature and tension. In contrast, the fusion of ellipsoidal micelles in the other two kinds of models cannot decrease the membrane curvature and tension to the maximum extent.

In principle, increasing DP of core-forming block and improving total solid content are commonly used strategies for promoting morphological transitions during PISA. Thus, the PISA of PDMAEMA$_{30}$–PHDFDMA$_{100}$ nano-objects at 30% solids contents was conducted. As indicated in Fig. 5A, micron-long tubes were generated, of which the average width of the tubes was around 102 nm and the width of the tube wall was 35 nm, respectively (Fig. S6†). Besides micro-long tubes, ellipsoidal vesicles (Fig. 5A) and the fusing dimer with a central wall (Fig. 5B) were also observed. The DLS results shown in Fig. 5D agree well with the morphological observations in Fig. 5A: the
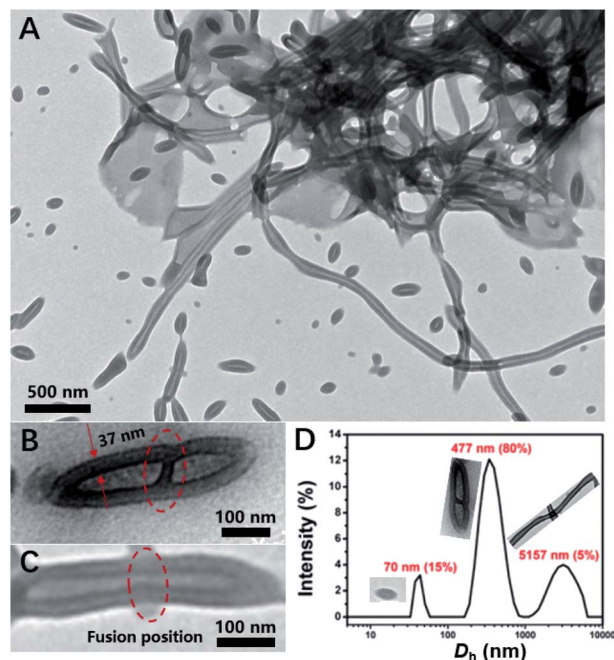
Fig. 5 (A) TEM micrograph of PDMAEMA$_{30}$–PHDFDMA$_{100}$ nano-objects in ethanol, 70 °C, 30% solids content; (B) TEM micrograph of fusing dimer with a central wall; (C) the central wall destabilized and retracted into the outer wall; (D) DLS of PDMAEMA$_{30}$–PHDFDMA$_{100}$ nano-objects in ethanol, 70 °C, 30% solids content.

peaks with 70, 477, and 5157 nm corresponded to small ellipsoidal vesicles, vesicle dimers, and micro-long tubes, respectively. Furthermore, the width of the tube wall was almost the same as that of a fused dimer (37 nm, Fig. 5B). Hence, combining these results, it can be rationally concluded that microtubes resulted from the directional fusion of ellipsoidal vesicles in a head-to-head model, which was schematically shown in Scheme 1C. Firstly, the two poles of the ellipsoidal vesicles preferred to contact and adhesive, resulting in a central wall within the vesicular dimer (Fig. 5B), which is in well agreement with the observation by Discher *et al.*[8] In this way, the molecular curvature of the ellipsoidal vesicles can be reduced to the maximum extent. Then, the central wall is destabilized and retracted into the outer wall, resulting in short tubes (Fig. 5C). Subsequently, the short tubes further fused with more ellipsoidal vesicles and eventually, formed micro-long tubes. Rationally, both ellipsoidal vesicles and the short tubes can be regarded as the precursors for long micro-tubes. An increase of just 5 HDFDMA units at 30% solids led to gradual transition from micro-tubes to rods as the cavities of tubes were gradually filled (Fig. S7 and S8†).

The LC nature of the PHDFDMA block is the main reason for the formation of unusual anisotropic morphology. Herein, the mesomorphic properties of PDMAEMA$_{30}$-*b*-PHDFDMA$_n$ nanostructures were analysed by using differential scanning calorimetry (DSC) and X-ray diffraction (XRD). As is shown in Fig. 6, diffraction peaks at 2.8°, 5.6°, 8.4°, and 17.9° correspond to four Bragg spacings (3.16, 1.58, 1.07, and 0.50 nm), among which the spacing of 1.58 nm can be assigned to the rod-like

Scheme 2 Schematic demonstration of a directional fusion of ellipsoidal morphology along the long axis driven by the molecular curvature.

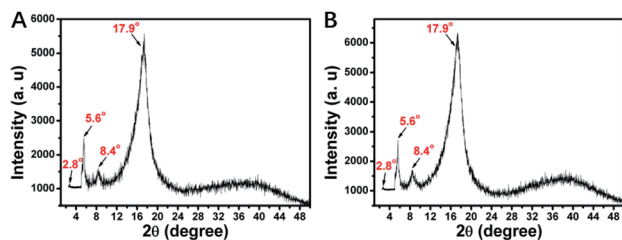Fig. 6 X-ray diffraction patterns for (A) PDMAEMA$_{30}$–PHDFDMA$_{50}$ and (B) PDMAEMA$_{30}$–PHDFDMA$_{100}$ fluoro-containing block copolymer nanoparticles.
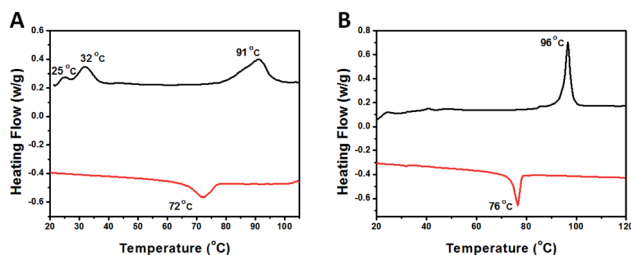
Fig. 7 DSC traces for (A) PDMAEMA$_{30}$–PHDFDMA$_{100}$ fluoro-containing block copolymer nano-objects and (B) PHDFDMA$_{50}$ homopolymer. The red and black lines refer to the heating half-cycle and cooling half-cycle, respectively.

perfluoroalkyl chain length.[51] This provides convincing evidence that HDFDMA blocks formed an ordered smectic B (SmB) phase. As Lv et al. reported, the temperature of polymerization (T_p) in PISA is crucial for morphological evolution because the mobility of core-forming block can be affected by T_p.[43] They found that when T_p of PISA was appropriately lower than or close to the glass transition temperature (T_g), the mobility of the core-forming block was retarded, facilitating the one-dimension fusion of vesicles into tubes. In our work, the T_p for all PISA formulations were set to be 70 °C, a commonly used temperature for most RAFT-PISA protocols. To check if the T_p we utilized is appropriately lower than or close to the SmB-to-isotropic phase transition temperature of PHDFDMA blocks, the DSC measurements were conducted. As indicated in Fig. 7, a SmB to isotropic phase transition at 72 °C for PDMAEMA$_{30}$–PHDFDMA$_{100}$ was revealed, suggesting that T_p at 70 °C is appropriate in our PISA system. In order to better explain directional fusion mechanism for ellipsoidal morphologies, we performed a PISA of PDMAEMA$_{30}$–PHDFDMA$_{100}$ with 20% solids content at 76 °C. TEM micrograph in Fig. S9† demonstrated that only spherical particles formed and no fusion of nanoparticles was observed. Since the T_p at 76 °C is higher than the SmB-to-isotropic phase transition temperature, the ellipsoidal morphologies were not produced and no directional fusion can be observed.

Conclusions

In summary, a directional effect on the fusion of ellipsoidal morphologies into nanorods and nanotubes was demonstrated

in our work. The ellipsoidal micelles and vesicles can be readily prepared via the dispersion polymerizations of HDFDMA mediated by PDMAEMA$_{30}$ due to the LC ordering of the SFLC blocks. In addition, the ellipsoidal morphologies preferred to fuse in a head-to-head manner, affording the lowest membrane curvature and tension. Thus, nanorods and nanotubes can be readily generated via the directional fusion of ellipsoidal micelles and vesicles, respectively. We believe the directional effect on nanoparticle fusion will offer insightful guidance to the preparation of complicated functional nanostructures.[44]

Experimental

Materials

2,2′-Azobis(2-methylpropionitrile) (AIBN, 99%) were purchased from Sigma-Aldrich. Heptadecafluorodecyl methacrylate (HDFDMA, 98%) and 2-(dimethylamino)ethyl methacrylate (DMAEMA, 99%) were purchased from Shanghai Aladdin Bio-Chem Technology. CDCl$_3$ (99.8%) was purchased from J&K Scientific. CF$_2$ClCFCl$_2$ (99.5%) was purchased from Shanghai Macklin Biochemical. All the monomers were passed through an Al$_2$O$_3$ column to remove the inhibitor prior to polymerizations. The chain transfer agent 4-cyano-4-(ethylthiocarbonothioylthio) pentanoic acid (CEPA) was synthesized according to a previously published procedure.[52]

Characterization

The monomer conversions (HDFDMA and DMAEMA) and chemical structure of the synthesized polymers, including PDMAEMA$_{30}$-CTA and PDMAEMA$_{30}$–PHDFDMA$_n$, were analyzed by ^{1}H NMR spectroscopy on a Bruker AV 400 MHz spectrometer. CF$_2$ClCFCl$_2$ was utilized as a cosolvent together with a suitable deuterated solvent to sufficiently dissolve fluoro-containing block copolymer nanoparticles. Gel permeation chromatography (GPC) measurements were performed on a Waters Alliance e2695 GPC system equipped with a Styragel guard column (WAT054415, 30 × 4.6 mm), two org separation columns consisting of D2500 (300 × 8 mm) and D5000 (300 × 8 mm). Detection was made with a 2414 refractive index detector (Waters Alliance), a Viscotek 302/305 UV detector (Malvern Instruments), and a Viscotek TDA 305-020 LALS/RALS detector (Malvern Instruments). DMF (HPLC grade, containing 1 mg mL^{-1} LiBr) was used as the eluent at a flow rate of 0.8 mL min^{-1}. GPC samples were prepared by dissolving 3–5 mg dry polymer powder in 1 mL DMF and filtered through a 0.20 μm Millipore filter. The temperature of the columns and detector was set at 65 °C and 45 °C, respectively. Analysis of molecular weight and dispersity was carried out using Empower 2 software against polymethyl methacrylate (PMMA) standards (molecular weight range 2.4 × 10^2 to 1.0 × 10^6 g mol^{-1}). Dynamic light scattering (DLS) analysis was performed on a Malvern ZS90 with a He–Ne laser (633 nm, 4 mW) at a 90° angle. The as-synthesized nanoparticle dispersions via PISA were diluted to 0.1% (1 mg mL^{-1}) in a disposable cuvette using ethanol and analyzed after 30 minutes. The viscosity was 1.748 cP and the refractive index was 1.366. The temperature for all DLS characterizations was 25 °C

and the equilibration time was 120 seconds. Autocorrelation functions were analyzed by the cumulants method to calculate the z-average hydrodynamic diameter and polydispersity index (PDI). The morphology of the nanoparticles was analyzed by transmission electron microscopy (TEM) conducted on a Jeol 200CX microscope (200 kV). Differential scanning calorimetry (DSC) was performed on a NETZSCH DSC214 instrument under N_2 protection at a scanning rate of 10 °C min^{-1}. X-ray diffraction (XRD) measurements were carried out on a Rigaku Dmax 2500 PC diffractometer using Cu Kα radiation ($\lambda = 0.154$ nm).

Synthesis of PDMAEMA$_{30}$ macro-chain transfer agent

Macromolecular chain transfer agent was synthesized according to a previously published procedure.[53] In brief, DMAEMA (3.14 g, 20.0 mmol), CEPA (0.132 g, 0.5 mmol), and AIBN (8.2 mg, 0.05 mmol) were added into a glass vial and subsequently dissolved in 6.5 mL DMF. After the solution was purged with nitrogen for 30 minutes, the glass vial was placed into an oil bath at 70 °C and stirred at 500 rpm. After 3 h of polymerization under nitrogen, the glass vial was removed from the oil bath and the resulting solution was exposed to air to terminate the polymerization. The monomer conversion was determined to be 70% by ^{1}H NMR spectroscopy. The polymer was purified in a dialysis bag (MWCO 1.0 kg mol^{-1}) against ethanol for two days. After rotary evaporation and drying under vacuum, polymer sample with high purity was obtained.

Synthesis procedure for the dispersion polymerization of HDFDMA mediated by PDMAEMA$_{30}$-CTA

A certain amount of PDMAEMA$_{30}$-CTA and HDFDMA were added into a glass vial and dissolved in ethanol. After the solution was degassed for 30 minutes in an ice bath, a certain amount of AIBN dissolved in ethanol was injected into the reaction mixture under N_2 atmosphere and the glass vial was placed into an oil bath at 70 °C with a stirring speed of 500 rpm. After a certain time of polymerization under nitrogen atmosphere, the glass vial was removed from the oil bath and the solution was exposed to air to terminate the polymerizations. The monomer conversion was determined by ^{1}H NMR spectroscopy in CDCl$_3$. Purified copolymers were obtained by precipitation in diethyl ether and drying under vacuum. The BCPs compositions were characterized by ^{1}H NMR spectroscopy in a mixture of CDCl$_3$/CF$_2$ClCFCl$_2$ (3 : 2, v/v). The actual repeat unit of HDFDMA was determined by comparing the integral of signal h' ($\delta = 4.30$ ppm) and h ($\delta = 4.14$ ppm).

Author contributions

Yahui Li, Qunzan Lu and Qiumeng Chen performed the experiments. Xuan Wu, Jianliang Shen and Liangliang Shen designed the project and performed the data analysis. Liangliang Shen wrote the paper. All authors discussed the results.

Conflicts of interest

There are no conflicts to declare.

Acknowledgements

References

1 Y. Mai and A. Eisenberg, *Chem. Soc. Rev.*, 2012, **41**, 5969–5985.
2 S. B. Darling, *Prog. Polym. Sci.*, 2007, **32**, 1152–1204.
3 A. Rosler, G. W. M. Vandermeulen and H.-A. Klok, *Adv. Drug Delivery Rev.*, 2012, **64**, 270–279.
4 J. Y. Cheng, A. M. Mayes and C. A. Ross, *Nat. Mater.*, 2004, **3**, 823–828.
5 F. H. Schacher, P. A. Rupar and I. Manners, *Angew. Chem., Int. Ed.*, 2012, **51**, 7898–7921.
6 A. O. Moughton, M. A. Hillmyer and T. P. Lodge, *Macromolecules*, 2012, **45**, 2–19.
7 H. Qiu, Y. Gao, C. E. Boott, O. E. C. Gould, R. L. Harniman, M. J. Miles, S. E. D. Webb, M. A. Winnik and I. Manners, *Science*, 2016, **352**, 697–701.
8 D. E. Discher and A. Eisenberg, *Science*, 2002, **297**, 967–973.
9 J. Cai, C. Li, N. Kong, Y. Lu, G. Lin, X. Wang, Y. Yao, I. Manners and H. Qiu, *Science*, 2019, **366**, 1095–1098.
10 R. C. Hayward and D. J. Pochan, *Macromolecules*, 2010, **43**, 3577–3584.
11 L. P. D. Ratcliffe, M. J. Derry, A. Ianiro, R. Tuinier and S. P. Armes, *Angew. Chem., Int. Ed.*, 2019, **58**, 18964–18970.
12 H. Sun, W. Cao, N. Zang, T. D. Clemons, G. M. Scheutz, Z. Hu, M. P. Thompson, Y. Liang, M. Vratsanos, X. Zhou, W. Choi, B. S. Sumerlin, S. I. Stupp and N. C. Gianneschi, *Angew. Chem., Int. Ed.*, 2020, **59**, 19136–19142.
13 F. Lv, Z. An and P. Wu, *Nat. Commun.*, 2019, **10**, 1–7.
14 J. Yeow and C. Boyer, *Adv. Sci.*, 2017, **4**, 1700137–1700151.
15 F. D'Agosto, J. Rieger and M. Lansalot, *Angew. Chem., Int. Ed.*, 2020, **59**, 8368–8392.
16 T. Lückerath, K. Koynov, S. Loescher, C. J. Whitfield, L. Nuhn, A. Walther, C. Barner-Kowollik, D. Y. W. Ng and T. Weil, *Angew. Chem., Int. Ed.*, 2020, **59**, 15474–15479.
17 X. Cheng, T. Miao, L. Yin, Y. Ji, Y. Li, Z. Zhang, W. Zhang and X. Zhu, *Angew. Chem., Int. Ed.*, 2020, **59**, 9669–9677.
18 A. Blanazs, J. Madsen, G. Battaglia, A. J. Ryan and S. P. Armes, *J. Am. Chem. Soc.*, 2011, **133**, 16581–16587.
19 S. J. Byard, M. Williams, B. E. McKenzie, A. Blanazs and S. P. Armes, *Macromolecules*, 2017, **50**, 1482–1493.
20 G. Mellot, J. -M. Guigner, L. Bouteiller, F. Stoffelbach and J. Rieger, *Angew. Chem., Int. Ed.*, 2019, **131**, 3205–3209.
21 X. Chen, L. Liu, M. Huo, M. Zeng, L. Peng, A. Feng, X. Wang and J. Yuan, *Angew. Chem., Int. Ed.*, 2017, **129**, 16768–16772.
22 B. Zhang, X. Lv, A. Zhu, J. Zheng, Y. Yang and Z. An, *Macromolecules*, 2018, **51**, 2776–2784.
23 Y. Ding, M. Cai, Z. Cui, L. Huang, L. Wang, X. Lu and Y. Cai, *Angew. Chem., Int. Ed.*, 2018, **57**, 1053–1056.
24 M. Cai, Y. Ding, L. Wang, L. Huang, X. Lu and Y. Cai, *ACS Macro Lett.*, 2018, **7**, 208–212.

25 L. Shen, Y. Li, Q. Lu, X. Qi, X. Wu and J. Shen, *Polym. Chem.*, 2020, **11**, 4208–4212.

26 L. Shen, Y. Li, Q. Lu, X. Qi, X. Wu, Z. Zhou and J. Shen, *Chem. Commun.*, 2020, **56**, 2411–2414.

27 S. Guan, W. Wen, Z. Yang and A. Chen, *Macromolecules*, 2020, **53**, 465–472.

28 S. Guan and A. Chen, *ACS Macro Lett.*, 2020, **9**, 14–19.

29 X. Zhang, S. Boisse, C. Bui, P.-A. Albouy, A. Brulet, M.-H. Li, J. Rieger and B. Charleux, *Soft Matter*, 2012, **8**, 1130–1141.

30 X. S. Wang, G. Guerin, H. Wang, Y. S. Wang, I. Manners and M. A. Winnik, *Science*, 2007, **317**, 644–647.

31 A. Hirao, K. Sugiyama and H. Yokoyama, *Prog. Polym. Sci.*, 2007, **32**, 1393–1438.

32 A. Vitale, R. Bongiovanni and B. Ameduri, *Chem. Rev.*, 2015, **115**, 8835–8866.

33 T. Soulestin, V. Ladmiral, F. D. Dos Santos and B. Améduri, *Prog. Polym. Sci.*, 2017, **72**, 16–60.

34 V. V. Volkov, N. A. Platé, A. Takahara, T. Kajiyama, N. Amaya and Y. Murata, *Polymer*, 1992, **33**, 1316–1320.

35 T. Shimizu, Y. Tanaka, M. Ohkawa, S. Kutsumizu and S. Yano, *Macromolecules*, 1996, **29**, 3540–3544.

36 X. Li, Y. Gao, X. Xing and G. Liu, *Macromolecules*, 2013, **46**, 7436–7442.

37 X. Li, B. Jin, Y. Gao, D. W. Hayward, M. A. Winnik, Y. Luo and I. Manners, *Angew. Chem., Int. Ed.*, 2016, **55**, 11392–11396.

38 M. Huo, D. Li, G. Song, J. Zhang, D. Wu, Y. Wei and J. Yuan, *Macromol. Rapid Commun.*, 2018, **39**, 1700840.

39 M. Huo, G. Song, J. Zhang, Y. Wei and J. Yuan, *ACS Macro Lett.*, 2018, **7**, 956–961.

40 S. Guan, C. Zhang, W. Wen, T. Qu, X. Zheng, Y. Zhao and A. Chen, *ACS Macro Lett.*, 2018, **7**, 358–363.

41 L. Shen, H. Guo, J. Zheng, X. Wang, Y. Yang and Z. An, *ACS Macro Lett.*, 2018, **7**, 287–292.

42 S. Varlas, R. Keogh, Y. Xie, S. L. Horswell, J. C. Foster and R. K. O'Reilly, *J. Am. Chem. Soc.*, 2019, **141**, 20234–20248.

43 F. Lv, Z. An and P. Wu, *Macromolecules*, 2020, **53**, 367–373.

44 J. Xiao and J. Du, *J. Am. Chem. Soc.*, 2020, **142**, 6569–6577.

45 Z. Zhuang, T. Jiang, J. Lin, L. Gao, C. Yang, L. Wang and C. Cai, *Angew. Chem., Int. Ed.*, 2016, **55**, 1–7.

46 H. Gao, L. Gao, J. Lin, Y. Lu, L. Wang, C. Cai and X. Tian, *Macromolecules*, 2020, **53**, 3571–3579.

47 X. Wang, C. A. Figg, X. Lv, Y. Yang, B. S. Sumerlin and Z. An, *ACS Macro Lett.*, 2017, **6**, 337–342.

48 J. Tan, H. Sun, M. Yu, B. S. Sumerlin and L. Zhang, *ACS Macro Lett.*, 2015, **4**, 1249–1253.

49 J. Yeow, J. Xu and C. Boyer, *ACS Macro Lett.*, 2015, **4**, 984–990.

50 S. Sugihara, A. Blanazs, S. P. Armes, A. J. Ryan and A. L. Lewis, *J. Am. Chem. Soc.*, 2011, **133**, 15707–15713.

51 A. M. Coclite, Y. Shi and K. K. Gleason, *Adv. Mater.*, 2012, **24**, 4534–4539.

52 W. Shen, Q. Qiu, Y. Wang, M. Miao, B. Li, T. Zhang, A. Cao and Z. An, *Macromol. Rapid Commun.*, 2010, **31**, 1444–1448.

53 A. Zhu, X. Lv, L. Shen, B. Zhang and Z. An, *ACS Macro Lett.*, 2017, **6**, 304–309.